Fluid mechanics approach to perfusion quantification: vasculature computational fluid dynamics simulation, quantitative transport mapping (QTM) analysis of dynamics contrast enhanced MRI, and application in nonalcoholic fatty liver disease classification

Qihao Zhang*, Xianfu Luo*, Liangdong Zhou, Thanh D. Nguyen, Martin R. Prince, Pascal Spincemaille, Yi Wang

Abstract— *Objective:* We quantify liver perfusion using quantitative transport mapping (QTM) method that is free of arterial input function (AIF). QTM method is validated in a vasculature computational fluid dynamics (CFD) simulation and is applied for processing dynamic contrast enhanced (DCE) MRI images in differentiating liver with nonalcoholic fatty liver disease (NAFLD) from healthy controls using pathology reference in a preclinical rabbit model. *Methods:* QTM method was validated on a liver perfusion simulation based on fluid dynamics using a rat liver vasculature model and the mass transport equation. In the NAFLD grading task, DCE MRI images of 7 adult rabbits with methionine choline-deficient diet-induced nonalcoholic steatohepatitis (NASH), 8 adult rabbits with simple steatosis (SS) were acquired and processed using QTM method and dual-input two compartment Kety's method respectively. Statistical analysis was performed on six perfusion parameters: velocity magnitude $|u|$ derived from QTM, liver arterial blood flow LBF_a, liver venous blood flow LBF_v, permeability K^{trans}, blood volume V_p and extravascular space volume V_e averaged in liver ROI. *Results:* In the simulation, QTM method successfully reconstructed blood flow, reduced error by 48% compared to Kety's method. In the preclinical study, only QTM |u| showed significant difference between high grade NAFLD group and low grade NAFLD group. *Conclusion:* QTM postprocesses DCE-MRI automatically through deconvolution in space and time to solve the inverse problem of the transport equation. Comparing with Kety's method, QTM method showed higher accuracy and better differentiation in NAFLD classification task. *Significance:* We propose to apply QTM method in liver DCE MRI perfusion quantification.

Index Terms—Kinetic modeling; Liver perfusion quantification; Magnetic resonance imaging; Quantitative transport mapping (QTM)

I. INTRODUCTION

DYNAMIC contrast enhanced MRI (DCE-MRI) captures the passage of contrast agent in tissues, which can reflect perfusion, vessel volume, and permeability information[1, 2]. Traditional quantitative analysis of DCE-MRI is based on Kety's equation [3], also referred to as Toft's model in MRI [4], where blood flow F and blood volume V_p can be calculated if arterial input function (AIF) is known[5]. Although various studies have revealed it's promising to use this traditional tracer kinetic modeling method in lesion classification, tumor grading and treatment response[6-8], Kety's model hasn't been commonly applied in clinical practice yet[9-11], largely due to variation in kinetic modeling[4, 5] and dependency of kinetic parameters on the choice of AIF[12]. Particularly, AIF for a voxel is not well defined in principle, as there may be several vessels input into that voxel, and it is nearly impossible to estimate an AIF for a voxel from DCE-MRI data in principle [13-15]. In practice, a single global AIF is often assumed to supply all voxels, ignoring voxel-level deviations from the global AIF in terms of dispersions; the AIF estimation from DCE-MRI suffers from partial volume effects and varies highly with the choice of location for AIF estimation[12].

The regional tissue blood flow can be determined by inverting the transport equation in a fully automated manner without any AIF input which is termed as quantitative transport mapping (QTM) [15-17]. Using a vascular tree CFD simulation to validate quantitative tissue perfusion, QTM is shown to be substantially more accurate than Kety's approach for kidney perfusion quantification[15]. Correlating with immunohistochemistry, QTM processing of DCE-MRI provides more significant resolutions of pathological markers than Kety's approach in nasopharyngeal carcinoma [18] and in breast cancer [19].

In this study, we intend to establish QTM processing of DCE MRI for liver perfusion quantification. To validate QTM method, we extend the vascular tree model for contrast agent transport simulation to a liver vasculature-tissue model[15]. To access potential clinical value of voxel average velocity

$|\boldsymbol{u}|$ derived from QTM, we compare both QTM and Kety's method with pathological classification of nonalcoholic fatty liver disease (NAFLD), the leading cause of chronic liver disease[20-24].

II. MATERIALS AND METHODS

We organize this section into the following subsections: A. review both Kety's and QTM postprocessing methods. B. Validation of Kety's and QTM method against CFD simulated flow as ground truth using CFD simulated tracer concentration as input. C. Application in NAFLD grading task.

A. Postprocessing methods for DCE MRI

Two postprocessing methods were implemented, traditional Kety's method using a global arterial input function, and quantitative transport mapping (QTM).

1) Traditional Kety's method

One-compartment kinetic modeling method was implemented in simulation:

$$\frac{\partial c(\boldsymbol{\xi},t)}{\partial t} = \text{LBF}(\boldsymbol{\xi})\left[c_a(t) - \frac{1}{V(\boldsymbol{\xi})}c(\boldsymbol{\xi},t)\right] \quad (1)$$

where $t \in \{1,2,...N_t-1\}$ the time index with N_t as the number of time frames, $\boldsymbol{\xi} = (\xi_x,\xi_y,\xi_z)$ is voxel index in a volume of (N_x,N_y,N_z) voxels along (x,y,z) axis, ∂_t is the time derivative, $c_a(t)$ is the tracer concentration of feeding artery (global AIF), LBF is liver blood flow, $V(\boldsymbol{\xi})$ is the volume fraction of vascular space, and $c(\boldsymbol{\xi},t)$ is the tracer concentration scalar field. Eq.1 is a linear equation system for LBF and $\frac{\text{LBF}}{\text{V}}$, and LBF can be solved using linear least squared method[25]. All the reconstruction is performed using MATLAB R2018a (Natick, Massachusetts: The MathWorks Inc.).

A two-compartment exchange model with dual inputs was also implemented for the liver DCE-MRI:

$$\frac{\partial V_p c_p(t)}{\partial t} = LBF_a c_a(t) + LBF_v c_v(t) - K_{ep}c_p(t) - K^{trans}c_p(t) + K^{trans}c_e(t) \quad (2)$$

$$\frac{\partial V_e c_e(t)}{\partial t} = K^{trans}c_p(t) - K^{trans}c_e(t) \quad (3)$$

Here $c_a(t)$ and $c_v(t)$ are arterial and portal vein input function, LBF_a and LBF_v are arterial and portal venous blood flow, K^{trans} is exchange rate between vascular and extravascular space, V_p and V_e are volume fraction of vascular and extravascular space, $c(t) = V_p c_p(t) + V_e c_e(t)$ is the tracer concentration in the voxel, and $K_{ep} = LBF_a + LBF_v$ is the outflux rate. Eq.2 and 3 was solved using linear least squared method[25].

2) Quantitative transport mapping

QTM method is used to reconstruct the flow velocity from the 4D contrast agent concentration profile. Given a time resolved 4D DCE-MRI data, its contrast agent concentration can be calculated by assuming a linear relationship between signal intensity change and contrast agent concentration [26]. In quantitative transport mapping, tracer concentration profile is modeled by transport equation [15, 27]:

$$-\nabla \cdot c(\boldsymbol{\xi},t)\boldsymbol{u}(\boldsymbol{\xi}) + \nabla \cdot D(\boldsymbol{\xi})\nabla c(\boldsymbol{\xi},t) = \partial_t c(\boldsymbol{\xi},t). \quad (4)$$

Here $\nabla = (\partial_x,\partial_y,\partial_z)$ the gradient operator, $\boldsymbol{u}(\boldsymbol{\xi}) = (u^x(\boldsymbol{\xi}),u^y(\boldsymbol{\xi}),u^z(\boldsymbol{\xi}))$ is an average velocity vector field with

magnitude $|\boldsymbol{u}(\boldsymbol{\xi})| = \sqrt{u^x(\boldsymbol{\xi})^2 + u^y(\boldsymbol{\xi})^2 + u^z(\boldsymbol{\xi})^2}$, and $D(\boldsymbol{\xi})$ the diffusion coefficient scalar field[26]. Both time derivative and gradient operator are difference operations in the discretized 4D spacetime-resolved image space. For DCE MRI scans that the images are acquired within 5 minutes after injection, the diffusion effect is much smaller than convection effect and cannot be accurately reconstructed from Eq.4, therefore can be neglected[27]. Eq.4 is a linear partial differential equation. The velocity is solved from an optimization problem with L1 total variation regularization as in a recent QTM study with the regularization parameters $\lambda = 10^{-3}$ chosen according to the L-curve method [15] :

$$\boldsymbol{u} = \underset{\boldsymbol{u}}{\text{argmin}} \sum_{t=1}^{N_t-1}\|\partial_t c + \nabla \cdot c\boldsymbol{u}\|_2^2 + \lambda\|\nabla\boldsymbol{u}\|_1. \quad (5)$$

Comparing with traditional kinetic modeling method, QTM method doesn't require AIF as input. In numerical simulation, $\boldsymbol{u}$ is converted to flow by multiplying with voxel cross section area and vascular space volume and compared with ground truth flow. In DCE MRI processing, we report nonalcoholic fatty liver disease and simple steatosis classification accuracy of $\boldsymbol{u}$ and traditional kinetic modeling output.

B. Validation against CFD simulation ground truth of contrast agent transport in liver

1) Liver perfusion simulation based on fluid dynamics

Our liver perfusion model contains three parts: supplying vascular system part (hepatic artery and portal vein, denoted by SVS), capillary system and homogenized hepatic space part (denoted by HHS) and draining vein system part (hepatic vein, denoted by DVS). For SVS and DVS, each artery and vein is assumed to a cylinder with parabolic flow running through, and flow rate is determined by Poiseuille's law. For HHS, capillary space and extravascular space are modeled as homogeneous porous media, and the flow velocity is determined by Darcy's law. Contrast agent concentration can then be simulated using CFD model given SVS&DVS structure, HHS volume and boundary concentration at artery inlet. In this study, we used vasculature and tissue volume from a 35um^3 resolution rat liver micro-CT scan, consisting of SVS and DVS geometry from the root of the vessel to its 11th branches[28]. Rat liver vasculature has similar branching pattern and perfusion value with human liver[29-31], therefore is commonly used for liver perfusion and drug delivery study. Details of the CFD simulation are described as follows, and all the computations below were performed on a computer with an Intel i7-8700K 6-core CPU and 64GB memory:

Assuming a cylinder shape for each vessel segment and a parabolic flow through the SVS and DVS vascular network, velocity and flow in each vessel segment and pressure at each connecting node can be calculated based on Poiseuille's law and boundary condition[32]:

$$\sum_{j \text{ connected to } i}\frac{\pi d_{ij}^4}{128\mu l_{ij}}(P_j - P_i) = 0, \ \ i \text{ is branching point} \quad (6)$$

$$\frac{\pi d_{ij}^4}{128\mu l_{ij}}(P_j - P_i) = F_0, i \text{ is terminal point} \quad (7)$$

Here i represents one specific node, j is the node connected to i, d_{ij} and l_{ij} are the diameter and length of the segment between i and j, and $\mu = 3 \times 10^{-3} \, Pa \cdot s$ is blood viscosity. If i is a branching point, the net flow through the node should be 0 (flow conservation). And if i is a terminal point, a constant flow F_0 as boundary condition is implied. In this study, we assumed a constant flow rate of 0.4mL/s at the root of SVS and DVS, and assumed the flow is evenly distributed to the terminals of SVS and DVS. The simulated average perfusion in liver is 62 mL/100g/min. The vasculature and flow in each segment are shown in Figure 1.

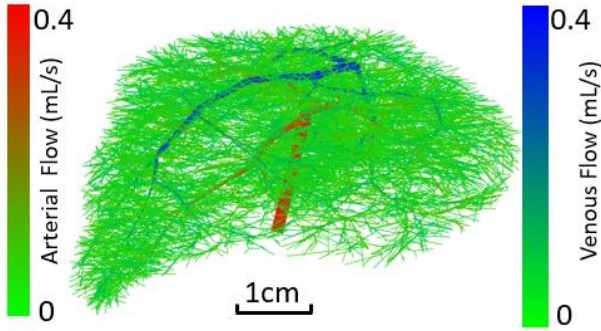After pressure at each connecting node is calculated, the flow

Figure 1. vessel segments for simulated liver blood flow

of the segment between node i and j can be calculated as $F_{ij} = \frac{\pi d_{ij}^4}{128\mu l_{ij}}(P_i - P_j)$, and the velocity at each point in the segment can be expressed as $u_{ij}(r) = \frac{2F_{ij}}{\pi R_{ij}^2}\left(1 - \frac{r^2}{R_{ij}^2}\right)$. Here, R_{ij} is the radii of the segment and r is the distance of the point to the axis of the cylinder. Tracer propagation in the vascular network can be simulated based on transport equation using finite element method[33]. To decrease the memory cost because of saving and computing the tracer concertation in all elements at each time step, 1D plug flow assumption is commonly used to simplify the computation[34]. However, plug flow assumption may introduce error when solving tracer propagation. We propose a tracer propagation approximation based on parabolic flow as follows:

Assuming parabolic flow inside each vessel segment and ignoring diffusion effect because it's small comparing with convection effect in vessel network[35], the concentration at each point can be expressed as $c(x,r,t) = c(0,r,t - \frac{x}{u(r)})$. Here x is the distance of the point to the start of the cylinder assuming the velocity direction is positive direction. At the bifurcation point, we assume the radial waveform is preserved:

$$c_{daughter}(0,r,t) = c_{father}\left(l_{father}, \frac{R_{father}}{R_{daughter}}r, t\right) \quad (8)$$

At the meeting point, we assume the concentration of father branch is the average of concentration in daughter branch weighted by its flow:

$$c_{father}(0,r,t) =$$
$$\sum_{all\ daughter\ branch} \frac{F_{daughter_i}}{F_{father}} c_{daughter_i}\left(l_{daughter_i}, \frac{R_{daughter_i}}{R_{father}}r, t\right) \quad (9)$$

In arterial side, father branch means the branch in upstream direction, while in venous side father branch means the branch in downstream direction. As flow is conserved at the connecting point, the concentration is also conserved. A concentration

input $c(t) = 0.28te^{-\frac{t}{45s}} + 9.1(1 - \exp(-\frac{t}{15s}))$ was applied at the arterial input for the simulation, which is acquired by fitting relative enhancement of hepatic artery (average value in a 9 voxel hepatic artery ROI) in a NAFLD rabbit DCE MRI scan to 4-parameter AIF $c(t) = k_1 te^{-\frac{t}{k_2}} + k_3(1 - \exp(-\frac{t}{k_4}))$ (red line in Figure 2b). Eqs.8&9 allow us to calculate the tracer concentration at each segment independently instead of updating all the segments at the same time and were solved at 1um spatial resolution and 1ms temporal resolution. The accuracy of this simulation in SVS and DVS is validated on a three-level vessel network where accurate tracer propagation simulation based on finite element method is performed using COMSOL Multiphysics (COMSOL AB, Stockholm, Sweden), which is shown in appendix 1.
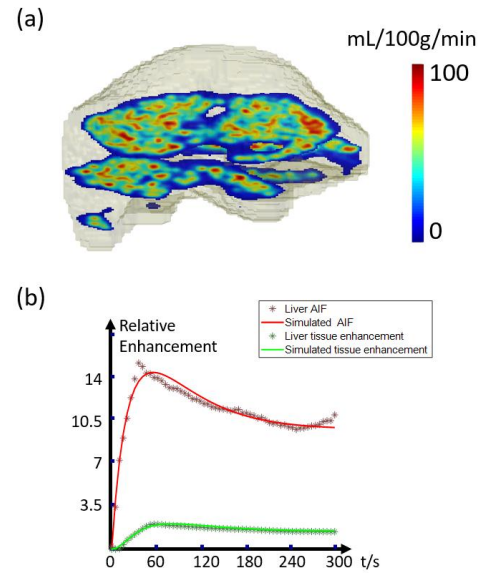

Figure 2. (a) liver blood flow in hepatic space. (b) AIF used in CFD simulation (red solid line) interpreted from measured AIF in rabbit hepatic artery (red stars); simulated hepatic tissue enhancement (green line) comparing with measured hepatic tissue enhancement (green stars) in a rabbit DCE MRI.

For the tracer transport in HHS, we employ a one compartment porous media model. Velocity and pressure in HHS (referred as volume V) are calculated based on Darcy's law[28]:

$$-\nabla \cdot (\alpha \nabla p) = g_{flow} \quad inside\ V \quad (10)$$
$$\partial_v p = 0 \ on\ the\ boundary\ of\ V \quad (11)$$
$$\boldsymbol{u} = \frac{\alpha}{\phi}\nabla p \quad (12)$$

Here g_{flow} is the flow source from SVS and flow sink form DVS. $\partial_v p$ is the gradient of pressure p vertical to liver surface. α is effective permeability defined as permeability divided by viscosity. α is set to 1 as velocity field $\boldsymbol{u}$ doesn't depend on α. $\phi = 0.15$ is the vascular space volume[36]. $\boldsymbol{u}$ is velocity vector and can be converted to flow by multiplying with ϕ and integrating on any surface area. Tracer concentration c in HHS can be simulated using transport equation based on the calculated velocity:

$$\frac{\partial c}{\partial t} = -\nabla \cdot (c\boldsymbol{u}) + g_c \quad (13)$$

Here g_c is the concentration source from SVS and concentration sink form DVS. Eqs.10-13 were discretized and

solved using finite volume method[33] implemented on MATLAB R2018a (Natick, Massachusetts: The MathWorks Inc.) at spatial resolution 0.5mm and temporal resolution 1ms. This simulation resolution was determined by computer memory, and the accuracy under this resolution is validated against a high-resolution tracer propagation simulation of porous media in a small volume, which is shown in appendix 2.

After tracer propagation in SVS, HHS and DVS was calculated, it was integrated in $0.5mm^3$ cubical voxels at 5s temporal resolution and was used as input for |u| and LBF reconstruction using QTM and Kety's method. For Kety's method, the concentration input at artery inlet ($c(t) = 0.28te^{-\frac{t}{45s}} + 9.1[1 - \exp{(-\frac{t}{15s})}]$) was used as AIF. The reconstruction accuracy was evaluated using relative root mean squared error (rRMSE), which is the L2 norm of the difference between prediction and ground truth divided by L2 norm of ground truth.

2) Application of QTM in pathological nonalcoholic fatty liver disease (NAFLD) classification

Based on the spectrum of steatosis, lobular inflammation, and hepatocyte ballooning, NAFLD can be divided into two categories: simple steatosis (SS) and nonalcoholic steatohepatitis (NASH). While patients with SS are at no higher risk of death than the general population, patients with NASH are at increased risk of death, as NASH may cause severe liver disease such as liver cirrhosis and hepatocellular carcinoma[37]. NASH is reversible after proper therapies to inhibit steatosis, inflammation[38, 39]. Therefore, detecting and staging of NAFLD is crucial to its treatment. Current golden standard for NAFLD classification is percutaneous liver biopsy[40]. However, it's not widely used in clinical assessments because of its invasiveness and variation because of the sampling position.

A preclinical animal model was used to test the clinical value of QTM in NAFLD grading task. Comparing with rats, rabbits are easier to feed and scan because of the size. Moreover, rabbit liver also has similar anatomical structure, vascular system, and perfusion value with human liver, thus is widely used in studying liver disease, especially when it's difficult to acquire pathology section in patients[41-44]. This study was approved by the animal care and use committee. 18 adult male New Zealand rabbits weighing from 2kg to 2.5 kg were included. All

Figure 3. Pathology image of a NASH case (a) and a SS case (b).

the rabbits were maintained at 21°C with a 12-hour light-dark cycle. The rabbits were randomly divided into 4 groups and were fed with a high fat/cholesterol diet (standard diet with additional 2% cholesterol and 10% triglycerides, Product No. TP2R144; Trophic Animal Feed High-tech Co. Ltd., China) for 4,6,8 and 10 weeks, respectively, to establish NAFLD. 3 rabbits died because of infection or anesthesia before measurement.

After the nurturing cycle, DCE-MRI scans of the remaining 15 rabbits were acquired on a GE Discovery 750 3T scanner with 3D spoiled gradient echo sequence (Liver Acquisition with Volume Acquisition, LAVA) before and after the injection of gadolinium contrast agent (Gd-DTPA-BMA, Omniscan, GE Healthcare, Ireland) using the following parameters: TR/TE 5.71/1.51 ms, voxel size $0.5 \times 0.5 \times 0.75$ mm^3, matrix size 256×256×36, flip angle 12°, temporal resolution 5s. 60 time points in total are acquired. The rabbits were anaesthetized to avoid motion. Registration between different time points was performed using FSL toolbox (FMRIB Software Library v6.0, Analysis Group, FMRIB, Oxford, UK.) to further remove respiratory motion. Region of interest (ROI) was drawn by an eight-year experienced radiologist in the middle of liver where the tissue was enhanced, and no obvious vessel can be observed. For two compartment exchange model perfusion parameter reconstruction, dual input function was applied. Arterial input was calculated as an average of 9 voxels in rabbit hepatic artery, and venous input was calculated as an average of 9 voxels in rabbit portal vein.
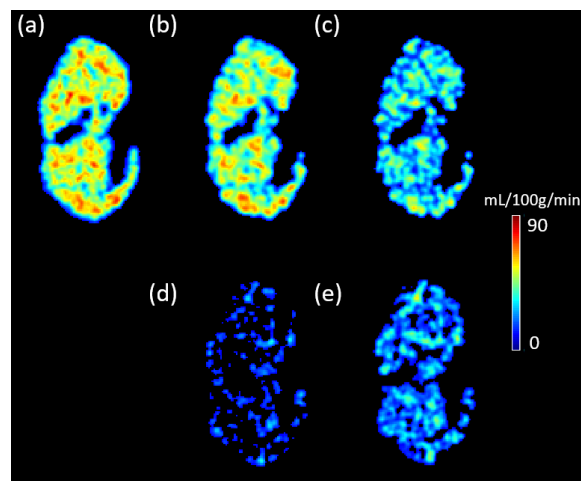

Figure 4. Liver blood flow reconstruction results: (a) ground truth, reconstructed with (b) QTM method and (c) Kety's method. Against the ground truth flow (a), QTM method showed a lower error (rRMSE 0.24 vs 0.46). (d) absolute error of QTM method and (e) absolute error of Kety's method.

Liver samples were firstly immersed in 10% phosphate-buffered formalin, then embedded in paraffin embedded and sectioned. All the sample slices were stained using hematoxylin, eosin, and Masson's trichrome and were reviewed by a pathologist with 15 years of experience blinded to the diet and imaging information. Each rabbit was scored by summing up semi-quantitatively determined indicators including steatosis (0–3 points), acinar inflammation (0–3 points) and hepatocellular ballooning (0–2 points) based on the NASH clinical research network's (NASH CRN) NAFLD Activity Score (NAS) system. In this study, 15 rabbits are divided into simple steatosis (SS) group (N=8, NAS=1,2) and nonalcoholic
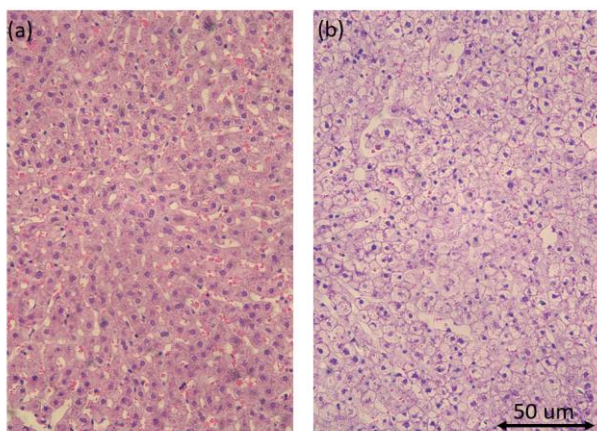
steatohepatitis (NAFH) group (N=7, NAS $\geq$ 3). One representative pathology slice of NASH and SS cases are shown in Figure 3, which correspond to the case shown in Figure 5 and 6.

Statistical analysis was performed on the perfusion parameters averaged in liver ROI. Using the R Statistical Software (Foundation for Statistical Computing, Vienna, Austria), a Mann-Whitney U test was performed comparing ROI values for $|\boldsymbol{u}|$, LBF_a LBF_v , K^{trans}, V_p and V_e between the two groups. Receiver operation curve (ROC) analysis was performed to test the discrimination accuracy of these perfusion parameters. P-values at or below 0.05 were considered to indicate statistical significance.
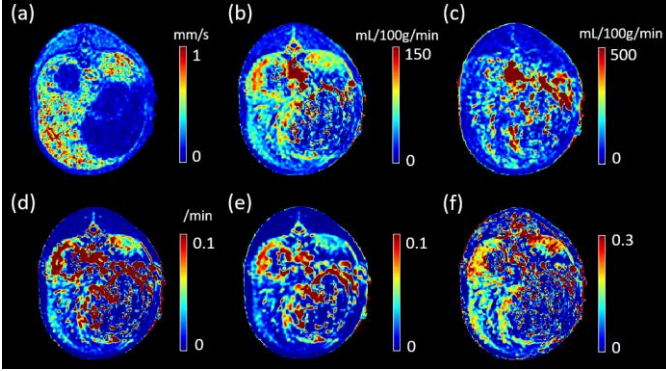

Figure 5. Perfusion parameters of a NASH case. a) QTM |u| map, b) LBF_a map, c) LBF_v map, d) K^{trans} map, e) V_p map and f) V_e map.
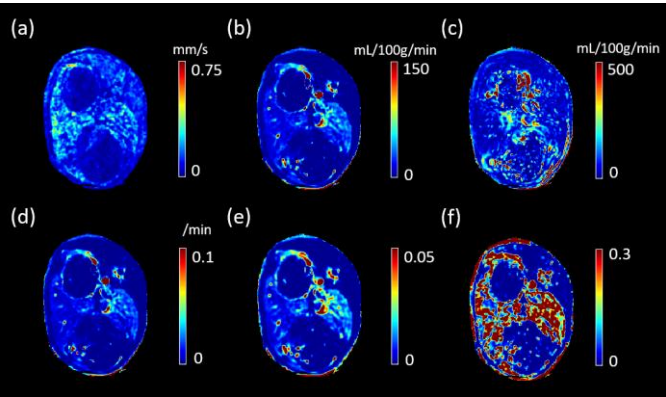

Figure 6. Perfusion parameters of a SS case. (a) QTM |u| map, (b) LBF_a map, (c) LBF_v map, (d) K^{trans} map, (e) V_p map and (f) V_e map
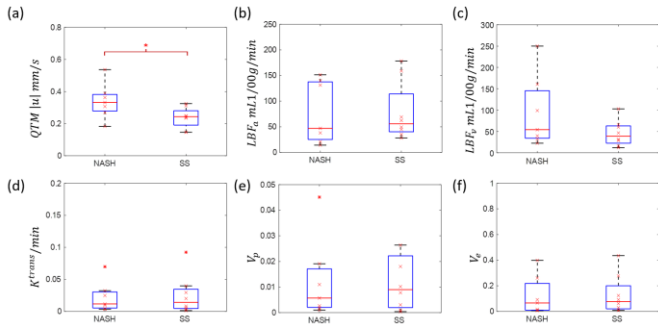

Figure 7. (a - f) NASH vs SS statistical comparison of QTM |u|, LBF_a,LBF_v,K^{trans},V_p and V_e respectively. A significant difference is observed on QTM |u| between NASH group and SS group.

III. RESULTS

A. CFD simulation

CFD simulated flow in vessels and hepatic tissue are shown in Figure 1 and 2: Figure 1 shows the flow in each vessel segment, and Figure 2a shows the flow magnitude in HHS at three cross sections of the liver. Tracer transport was then solved based on transport equation (Eqs.8,9 &13) using arterial input function approximated from the tracer concentration measured in hepatic artery, and the simulated tracer concentration profile in hepatic tissue was shown in Figure 2b.

$\boldsymbol{u}$ and LBF ware then reconstructed based on Eqs.1 and 5 using the simulated 4D tracer concentration image. The output $\boldsymbol{u}$ was converted to flow by multiplying the voxel surface area divided by plasma volume ϕ. Comparing with ground truth (Figure 4a), QTM method showed 60% reduction in error (Figure 4b and 4d, rRMSE=0.24) than Kety's method (Figure 4c and 4e, rRMSE=0.46), indicating the feasibility of applying QTM method into liver perfusion quantification.

B. Rabbit DCE-MRI experiment

T1 weighted DCE-MRI images were acquired on all 15 rabbits and were used to calculate the perfusion parameters using both QTM method and two-compartment Kety's parameters (Eqs 2,3 & 5). Perfusion parameter map of a representative NASH case and a SS case are shown in Figure 5 and 6, respectively. NASH case showed a higher |u|, K^{trans} and V_p comparing with SS case.

Statistically, a significant difference is observed between SS group and NAFH group in QTM |u| (0.18±0.08 mm/s vs 0.08±0.05 mm/s, p=0.04, AUC=0.82), but not in LBF_a (78.50±57.38 mL/100g/min vs 77.67±61.53 mL/100g/min, p=0.61, AUC=0.59), LBF_v (71.47±27.04 mL/100g/min vs 137.95±85.91 mL/100g/min, p=0.09, AUC=0.76), K^{trans} (0.025±0.014 /min vs 0.023±0.012/min, p=0.86, AUC=0.54), V_p (0.017±0.009 vs 0.013±0.006, p=1, AUC=0.50), and V_e (0.24±0.16 vs 0.16±0.10,p=0.28, AUC=0.68). Details of the ROC analysis is shown in appendix 9.

IV. DISCUSSION

Our results demonstrate the feasibility to quantify liver perfusion using QTM method. In the numerical simulation, QTM method showed higher accuracy in flow quantification comparing with traditional Kety's kinetic modeling method. In NAFLD grading task, significant difference of QTM velocity is found between SS group and NASH group, and no difference of LBF_a , LBF_v , K^{trans} , V_p and V_e is found between these groups, suggesting that velocity magnitude derived from QTM method has the potential to differentiate NASH from SS, and may perform better than kinetic parameters derived from traditional dual input two compartment exchange model[45]. This finding is consistent with liver vascular changes caused by steatosis and inflammation in NAFLD; this finding warrants clinical translational study in patients to address current lack of accurate noninvasive classification methods [46].

Perfusion quantification is highly promising to capture the changes in liver vascular morphology and flow during the

progression of NAFLD. Steatosis may decrease blood flow by increasing the resistance in vascular network[47], while liver fibrosis may increase the portal venous flow[48]. This change may be captured by dynamic imaging of tracer transport through liver and quantitative perfusion modeling. However, the output of traditional Kety's kinetic modeling method largely depends on the choice of AIF[49]. QTM method doesn't require arterial input function as an input, thus provides an automatic flow velocity evaluation method and is proven promising in the NAFLD grading task. The classification accuracy of QTM method may be further improved by a better estimation of contrast agent concentration and a higher resolution DCE MRI image[50]. Moreover, texture analysis may be used to improve the NAFLD detection [51]. Logistic regression may be used to combine these image measurements as well as laboratory test results to archive a better accuracy and specificity. This QTM development would be valuable for various noninvasive imaging techniques, such as ultrasound, MRI and CT, used in first-line investigation of NAFLD by detecting liver steatosis[52-54], particularly for establishing an accurate noninvasive alternative to biopsy for NAFLD detection and grading[55].

There are substantial technical advancements in the liver flow and tracer transport simulation used in this study. Compared to the vascular tree model used in the recent QTM validation in the kidney, the liver vasculature here based on experimental data is more complex and realistic with both artery part and venous part. This suggests that the fluid mechanics approach to tissue perfusion may be scaled to any organ tissue. There have been CFD studies for liver perfusion and drug delivery (16-18) using microvascular network (15,17,19), which can serve as a ground truth for validating tissue perfusion quantification (15,20) through integration of microvasculature over a voxel for interpreting the contrast agent concentration changes in space and time (21). However, these studies use plug flow for vascular branches, possibly due to limitations in memory and computational power [28, 56]. If the ground truth flow is parabolic, this plug flow assumption may cause around 10% error in tracer flux calculation, as first shown in this study.

Although liver perfusion quantification has been widely studied using Kety's kinetic modeling [57, 58], the calculated perfusion parameters has not yet been compared with ground truth in experimental measurements or simulation that are very difficult to perform. In this study, we present microvasculature CFD based simulation of tissue transport as ground truth. The accuracies of various DCE-MRI postprocessing methods can be validated on the correspondingly simulated 4D tracer propagation images against the ground truth. Here, we showed that there was substantial error in flow estimation using traditional Kety's kinetic modeling method. One possible reason is that traditional kinetic modeling method ignores the dispersion caused by tracer transport in arterial system. Transport equation is a more proper way to model the tracer propagation process[59].

In this study, we ignored the diffusion term in the vascular space (Eq.8). The diffusion coefficient of Gd in blood is around $3 \times 10^{-4} mm^2/s$[35], which is very small during observation time compared to the flow speed in vasculature network varies from 0.5mm/s to 100cm/s. Therefore, the diffusive flux is much smaller than convective flux, therefore can be neglected in flow simulation of vasculature networks. The analytical solution of parabolic flow transport process can be derived by assuming the tracer waveform is preserved when it travels from father branch to daughter branches, which allows a tracer transport simulation with error smaller than 1%. Moreover, no extra memory is needed, because global update of tracer concentration is vascular system is not needed.

There are several limitations of this study. First, constrained by the resolution of micro-CT, capillaries are not included in the vasculature model, therefore perfusion in hepatic space is modeled as flow in porous media. Liver vasculature acquired with higher resolution imaging techniques may be used to improve the accuracy of simulation. Second, vessels are considered as straight cylinders in this study, and blood is considered as incompressible fluid with low Reynolds number. In this situation, the flow in vessel network can be approximated as parabolic flow. Whether this assumption holds in curved vessels with varying radii and blood with high Reynolds number still need to be validated. Third, QTM model used in this study only contains one compartment. Hepatic sinusoidal capillaries are permeable to macromolecules such as gadolinium because of the large fenestrae on the vessel wall[60]. After gadolinium leaves capillary system, it will travel with interstitial fluid flow and may be collected by capillary system again[61]. The interstitial fluid flow speed is much smaller than capillary flow speed, and therefore a two-compartment exchange QTM model should be developed to better map the transport of contrast agent and compared with Kety's method. Fourth, the reconstruction accuracy of QTM method and Kety's method depend on spatial and temporal resolution, which should be discussed in the future work to determine the optimal acquisition resolution for perfusion parameter estimation. Fifth, gadolinium concentration ([Gd]) was estimated from DCE-MRI signal magnitude according to a linear model. The relationship between [Gd] and MRI signal magnitude is highly complex and affected by inflow effects[62]. Quantitative susceptibility mapping based on simple static magnetism for MRI signal phase processing offers a robust accurate alternative[63-65]. Sixth, high spacetime resolution 4D DCE-MRI is desired for QTM input to capture the full transport through the liver. Fast imaging can be employed for adequate spatial and temporal resolution[66-68]. Respiratory motion during imaging may be substantial and require effective motion compensation[69-71]. Seventh, the data size of the animal experiment is small (N=15). A larger dataset will be helpful for a precise evaluation about whether QTM can be used in early detection of NAFLD, which is important in clinical practice.

V. CONCLUSION

Both CFD simulation and preclinical imaging demonstrate that QTM is superior to Kety for liver perfusion quantification from DCE MRI data. |u| derived from QTM is promising in NAFLD grading task. Clinical study with a larger data size is warranted to compare the performance of QTM method against traditional Kety's kinetic modeling method and evaluate the possibility of coupling QTM in current non-invasive NAFLD grading assessment.

VI. APPENDIX

1) Validation of transport simulation in SVS and DVS

A three-level vasculature model was constructed to validate our flow and tracer concentration simulation method (shown in Figure A1a). The length and radii of the vessel segment for each level are 1mm, 1mm, 0.7mm and 0.1mm, 0.0794mm, 0.0630mm, respectively. The included angle of level2 and
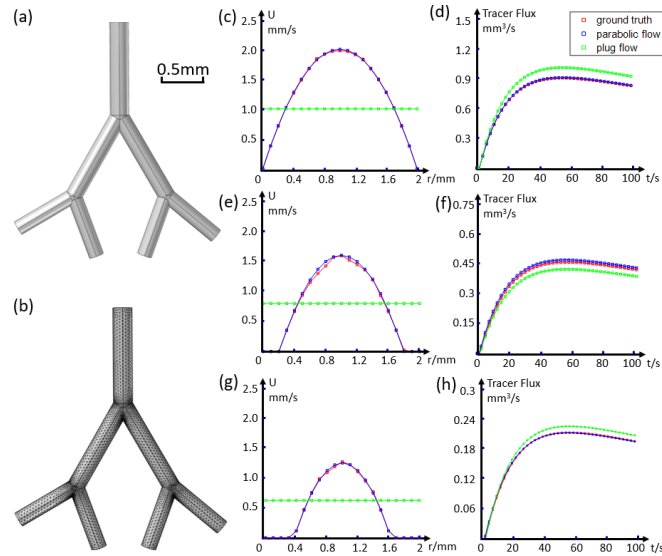

Figure A1. (a) structure of 3 level tube used to validate the parabolic flow simulation method. (b) the corresponding finite element mesh. (c), (e) and (g) ground truth velocity profiles (solid line) comparing with velocity profile simulated using plug flow (green dots) and parabolic flow assumption (blue dots) in radii direction at the middle cross section of level 1, 2 and 3 respectively. (d), (f) and (h) ground truth tracer fluxes (solid line) comparing with tracer flux simulated using plug flow (green dots) and parabolic flow assumption (blue dots) at the middle cross section of level 1, 2 and 3, respectively.

level3 vessels are 60° and 80°. Parabolic flow with maximum velocity 2mm/s is set as inlet boundary condition and zero pressure is set as outlet boundary condition. The diffusion coefficient is set to $3 \times 10^{-4}\ mm^2/s$[35]. Flow and velocity inside the vasculature were solved based on Navier-Stokes equation and transport equation using finite element method. Velocity in radial direction and tracer flux rate change with time were sampled at the middle point of the segment at each level.

We observed a high accuracy for flow simulation using parabolic flow assumption. Comparing with plug flow
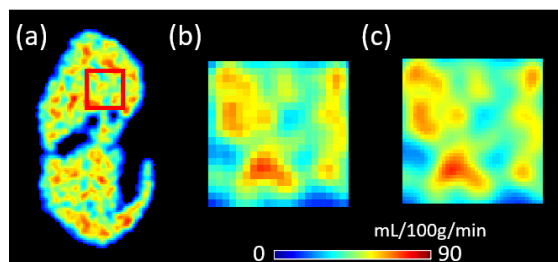

Figure A2. perfusion simulation in 10mm³ volume (red box in a) using 0.5mm grid size (figure b) and 0.25mm grid size (figure c). The difference in concentrations between the two resolutions is 4%.

assumption, parabolic flow assumption provides a more accurate velocity estimation (shown in Figure A1c, A1e and A1g), and decreased the tracer flux estimation error from 11%

with plug flow simulation to 0.5% (shown in Figure A1d, A1f and A1h).

2) Validation of transport simulation in HHS

For transport simulation in HHS, we used spatial resolution 0.5mm, which is determined by computer memory. We tested the simulation accuracy under this resolution by simulating a small volume with higher spatial resolution: 10mm cubical volume was chopped from the liver volume (shown in Figure A2) and tracer propagation was simulated with 0.25mm grid size. The difference between simulated tracer concentrations at the two resolutions was 4%, indicating the spatial resolution used is enough for accurate simulation.

3) QTM and Kety's reconstruction in simulation with noise

We tested QTM and Kety's reconstruction in simulation data described in main test with Gaussian noise (SNR=40, while the SNR of acquired DCE MRI is around 80). Reconstructed perfusion parameter map is shown in Figure A3. The rRMSE of QTM method is 24%, while the rRMSE of Kety's method is 46%.
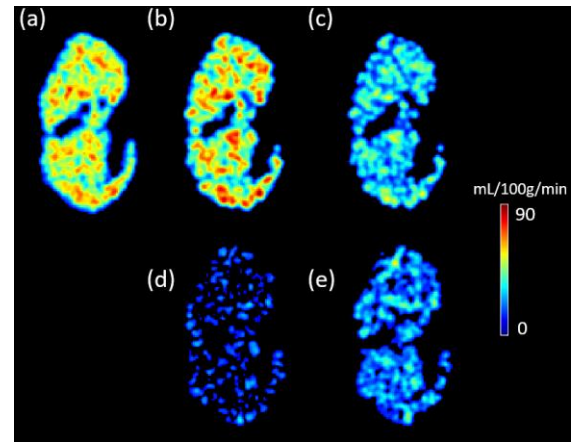

Figure A3 Liver blood flow reconstruction results with SNR=40 image: (a) ground truth, reconstructed with (b) QTM method and (c) Kety's method. Against the ground truth flow (a), QTM method showed a lower error (rRMSE 0.24 vs 0.46). (d) absolute error of QTM method and (e) absolute error of Kety's method.
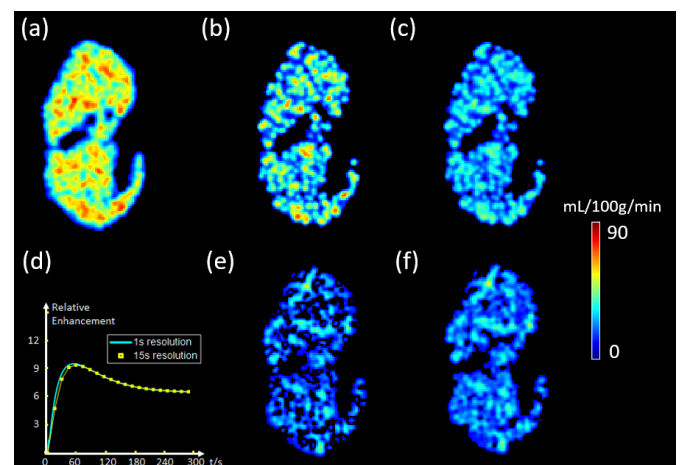

Figure A4. Liver blood flow reconstruction using Kety's method with AIF sampled at different temporal resolution: (a) ground truth flow, (b) Kety's method with 1s temporal resolution and (c) Kety's method with 15s temporal resolution. (d) AIF sampled at 1s and 15s resolution, (e) absolute error of Kety's method at 1s resolution and (f) absolute error of Kety's method at 15s resolution.

4) Kety's reconstruction in simulation with AIF sampled at different temporal resolution

We tested Kety's reconstruction in simulation data with AIF sampled at different temporal resolution. AIF sampled at 1s and 15s resolution is shown in Figure A4d. Kety's flow reconstruction error is 42% using AIF sampled at 1s resolution, and Kety's flow reconstruction error is 48% using AIF sampled at 15s resolution.

5) Reconstruction of liver DCE MRI using two compartment exchange model (2CXM) with population-based AIF

We tested Kety's reconstruction using population based AIF by fitting measured AIF to the following 4-parameter model using Levenberg-Marquardt method:

$$c_a(t) = k_1 t e^{-\frac{t}{k_2}} + (1 - k_3)e^{-\frac{t}{k_4}} \quad (A1)$$

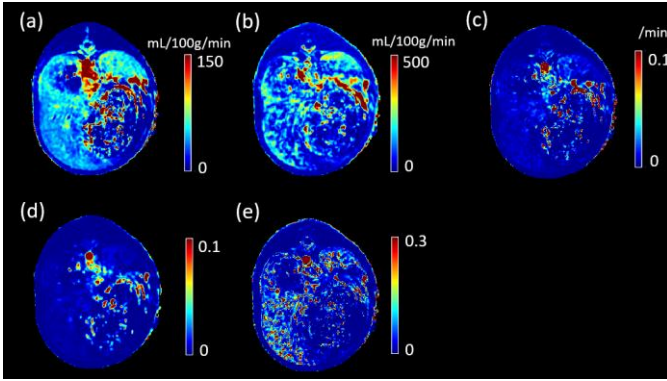Parameter map estimated from a NAFH group is shown in figure A5:

Figure A5. Perfusion parameters of a NASH case reconstructed using Kety's method with population based AIF. a) LBF_a map, b) LBF_v map, c) K^{trans} map, d) V_p map and e) V_e map.

Statistically, there is no difference between NASH and SS group for LBF_a (96.51 ± 85.42 vs 80.84 ± 78.92, p=0.86), LBF_v (112.82 ± 72.18 vs 80.57 ± 57.86, p=0.39), PS ($0.020/min \pm 0.014/min$ vs 0.006 ± 0.005, p=0.28), V_p (0.012 ± 0.010 vs 0.005 ± 0.004, p=0.23) and V_e (0.20 ± 0.19 vs 0.08 ± 0.05, p=0.23).
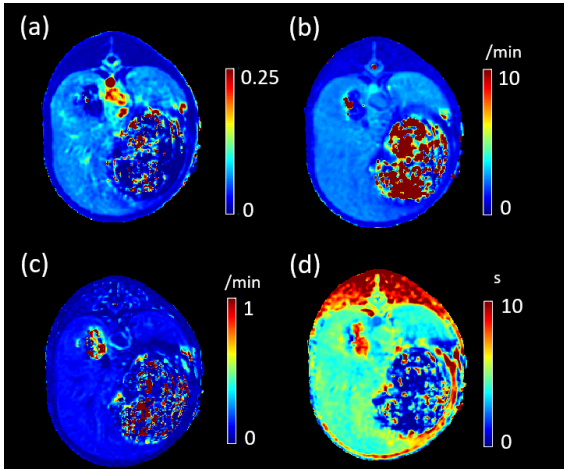

Figure A6. Perfusion parameters of a NASH case reconstructed using Brix model. a) AH map, b) K_{ep} map, c) K_{el} map, d) TA map.

6) Reconstruction of liver DCE MRI using Brix model

In Brix model, tracer propagation is modeled using the following equation[72, 73]:

$$C(t) = -\frac{AH}{K_{ep} - K_{el}}\left[e^{-K_{ep}(t-TA)} - e^{-K_{el}(t-TA)}\right] \quad (A2)$$

Here $C(t)$ is tracer concentration of tissue, TA is tracer arrival time, AH is magnitude scaling factor. K_{el} is the elimination constant of plasma and K_{ep} is the exchange rate of plasma and extravascular extracellular space. Eq.A2 was fitted using Levenberg-Marquardt method, and parameter map estimated from a NAFH group is shown in Figure A6.

Statistically, there is no difference between NASH and SS group for AH (0.04 ± 0.01 vs 0.04 ± 0.02, p=0.39), K_{ep} (2.14 ± 0.51 vs 2.17 ± 0.30, p=1), K_{el} (0.18 ± 0.06 vs 0.16 ± 0.09, p=0.34) and TA (0 ± 0.01 vs 0.99 ± 0.01, p=0.24).

7) Reconstruction of liver DCE MRI using adiabatic approximation of tissue homogeneity (TH) model

In adiabatic approximation of tissue homogeneity model, tracer propagation is modeled using the following equation[74]:

$$C(t) = V_{ai}C_a(t) + V_{vi}C_v(t) + EF_a(C_a(t)\otimes e^{-\frac{EF_a}{V_e}t}) + EF_v(C_v(t)\otimes e^{-\frac{EF_v}{V_e}t}) \quad (A3)$$

Here $C(t)$ is tracer concentration of tissue, V_{ai} and V_{vi} are product of arterial and venous blood flow with tracer transit time, EF_a and EF_v are product of arterial and venous blood flow with tracer extraction factor to extravascular extracellular space, and V_e is extravascular extracellular space volume. Eq.A3 was fitted using Levenberg-Marquardt method, and parameter map estimated from a NAFH group is shown in figure A7:
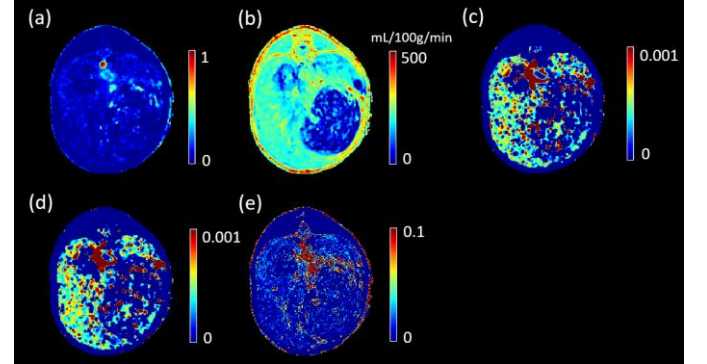

Figure A7. Perfusion parameters of a NASH case reconstructed using tissue homogeneity model. a) V_{ai} map, b) V_{vi} map, c) EF_a map, d) EF_v map and e) V_e map.

Statistically, there is no difference between NASH and SS group for V_{ai} (0.10 ± 0.05 vs 0.09 ± 0.04, p=1), V_{vi} (0.36 ± 0.09 vs 0.39 ± 0.12, p=0.77), EF_a (0.002 ± 0.001 vs 0.004 ± 0.002, p=0.77), EF_v (0.002 ± 0.001 vs 0.004 ± 0.002, p=0.69) and V_e (0.06 ± 0.02 vs 0.06 ± 0.04, p=0.86).

8) Reconstruction of liver DCE MRI using AIF-free reference tissue model

In reference tissue model, tracer propagation is modeled using the following equation[75, 76]:

$$C(t) = \frac{K^{trans}}{K_{RR}^{trans}}C_{RR}(t) + \frac{K^{trans}}{V_{e,RR}}\int_0^t C_{RR}(\tau)d\tau - K_{ep}\int_0^t C(\tau)d\tau \quad (A4)$$

Here $C(t)$ is tracer concentration of tissue, $C_{RR}(t)$ is tracer concentration of reference region. Eq.S4 was solved using a linear inversion method to estimate relative volume transfer
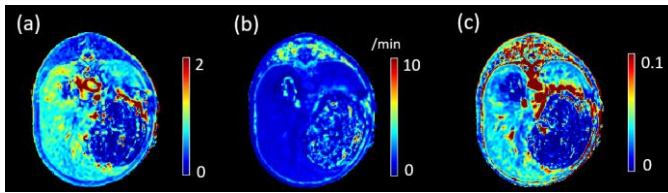
Figure A8 Perfusion parameters of a NASH case reconstructed using reference tissue model. a) $\frac{K^{trans}}{K^{trans}_{RR}}$ map, b) k_{ep}. Map, c) $\frac{V_e}{V_{e,RR}}$ map.

constant $\frac{K^{trans}}{K^{trans}_{RR}}$, relative extravascular extracellular space volume $\frac{V_e}{V_{e,RR}}$, and reflux time constant K_{ep}. Averaged tracer concentration of 9 voxels in muscle tissue near liver was used as reference tissue region. Parameter map estimated from a NAFH group is shown in Figure A8.

Statistically, there is no difference between NASH and SS group for relative volume transfer constant (0.77 ± 0.35 vs 0.51 ± 0.31, p=0.12), relative extravascular extracellular space volume (0.02 ± 0.01 vs 0.02 ± 0.01, p=0.54), and reflux time constant (0.58 ± 0.20 /min vs 0.44 ± 0.23/min, p=0.23).

9) Details of the ROC analysis of NAFLD differentiation task

In ROC analysis of NAFLD differentiation task, QTM |u| showed AUC=0.82 (95% confidence interval C 0.46 to 1) with sensitivity 0.86 (CI 0.33 to 1), specificity 0.75 (CI 0.33 to 1), optimal threshold 0.27mm/s (calculated by maximizing sensitivity plus specificity); LBF_a showed AUC=0.59 (CI 0.24 to 0.89), sensitivity 0.87 (CI 0.43 to 1), specificity 0.29 (CI 0 to 0.75), optimal threshold 35.97mL/100g/min; LBF_v showed AUC=0.76 (CI 0.35 to 0.96), sensitivity 0.57 (CI 0.16 to 1), specificity 0.87 (CI 0.42 to 1), optimal threshold 112.84mL/100g/min; K^{trans} showed AUC=0.54 (CI 0.18 to 0.84), sensitivity 0.85 (CI 0.28 to 1), specificity 0.25 (CI 0 to 0.67), optimal threshold 0.04/min; V_p showed AUC=0.50 (CI 0.19 to 0.80), sensitivity 0.85 (CI 0 to 1), specificity 0.25 (CI 0 to 0.67), optimal threshold 0.003; V_e showed AUC=0.68 (CI 0.30 to 0.91), sensitivity 0.75 (CI 0.26 to 1), specificity 0.71 (CI 0.25 to 1), optimal threshold 0.20.

VII. References

[1] J. O'Connor, P. Tofts, K. Miles, L. Parkes, G. Thompson, and A. Jackson, "Dynamic contrast-enhanced imaging techniques: CT and MRI," *The British journal of radiology,* vol. 84, no. special_issue_2, pp. S112-S120, 2011.

[2] P. S. Tofts, and A. G. Kermode, "Measurement of the blood‐brain barrier permeability and leakage space using dynamic MR imaging. 1. Fundamental concepts," *Magnetic resonance in medicine,* vol. 17, no. 2, pp. 357-367, 1991.

[3] S. S. Kety, "The theory and applications of the exchange of inert gas at the lungs and tissues," *Pharmacol Rev,* vol. 3, no. 1, pp. 1-41, Mar, 1951.

[4] P. S. Tofts, "Modeling tracer kinetics in dynamic Gd‐DTPA MR imaging," *Journal of magnetic resonance imaging,* vol. 7, no. 1, pp. 91-101, 1997.

[5] S. P. Sourbron, and D. L. Buckley, "On the scope and interpretation of the Tofts models for DCE‐MRI," *Magnetic resonance in medicine,* vol. 66, no. 3, pp. 735-745, 2011.

[6] R. G. Abramson, L. R. Arlinghaus, J. A. Weis, X. Li, A. N. Dula, E. Y. Chekmenev, S. A. Smith, M. I. Miga, V. G. Abramson, and T. E. Yankeelov, "Current and emerging quantitative magnetic resonance imaging methods for assessing and predicting the response of breast cancer to neoadjuvant therapy," *Breast cancer: targets and therapy,* vol. 4, pp. 139, 2012.

[7] A. G. Sorace, S. C. Partridge, X. Li, J. Virostko, S. L. Barnes, D. S. Hippe, W. Huang, and T. E. Yankeelov, "Distinguishing benign and malignant breast tumors: preliminary comparison of kinetic modeling approaches using multi-institutional dynamic contrast-enhanced MRI data from the International Breast MR Consortium 6883 trial," *Journal of Medical Imaging,* vol. 5, no. 1, pp. 011019, 2018.

[8] S. C. Agner, S. Soman, E. Libfeld, M. McDonald, K. Thomas, S. Englander, M. A. Rosen, D. Chin, J. Nosher, and A. Madabhushi, "Textural kinetics: a novel dynamic contrast-enhanced (DCE)-MRI feature for breast lesion classification," *Journal of digital imaging,* vol. 24, no. 3, pp. 446-463, 2011.

[9] Y.-H. H. Hsu, G. Z. Ferl, and C. M. Ng, "GPU-accelerated nonparametric kinetic analysis of DCE-MRI data from glioblastoma patients treated with bevacizumab," *Magnetic resonance imaging,* vol. 31, no. 4, pp. 618-623, 2013.

[10] N. Zhang, L. Zhang, B. Qiu, L. Meng, X. Wang, and B. L. Hou, "Correlation of volume transfer coefficient Ktrans with histopathologic grades of gliomas," *Journal of Magnetic Resonance Imaging,* vol. 36, no. 2, pp. 355-363, 2012.

[11] T. J. Yun, C.-K. Park, T. M. Kim, S.-H. Lee, J.-H. Kim, C.-H. Sohn, S.-H. Park, I. H. Kim, and S. H. Choi, "Glioblastoma treated with concurrent radiation therapy and temozolomide chemotherapy: differentiation of true progression from pseudoprogression with quantitative dynamic contrast-enhanced MR imaging," *Radiology,* vol. 274, no. 3, pp. 830-840, 2015.

[12] V. C. Keil, B. Mädler, R. Gieseke, R. Fimmers, E. Hattingen, H. H. Schild, and D. R. Hadizadeh, "Effects of arterial input function selection on kinetic parameters in brain dynamic contrast-enhanced MRI," *Magnetic resonance imaging,* vol. 40, pp. 83-90, 2017.

[13] F. Calamante, "Arterial input function in perfusion MRI: a comprehensive review," *Prog Nucl Magn Reson Spectrosc,* vol. 74, pp. 1-32, Oct, 2013.

[14] P. Spincemaille, Q. Zhang, T. D. Nguyen, and Y. Wang, "Vector field perfusion imaging." p. 3793.

[15] L. Zhou, Q. Zhang, P. Spincemaille, T. D. Nguyen, J. Morgan, W. Dai, Y. Li, A. Gupta, M. R. Prince, and Y. Wang, "Quantitative transport mapping (QTM) of the kidney with an approximate microvascular network," *Magn Reson Med*, Nov 18, 2020.

[16] Q. Zhang, L. Zhou, J. Morgan, T. Nguyen, P. Spincemaille, and Y. Wang, "Quantitative Transport Mapping (QTM): Inverse Solution to a Voxelized Equation of Mass Flux of Contrast Agent in a Porous Tissue Model." p. P37.

[17] Q. Zhang, L. Zhou, J. Morgan, T. Nguyen, P. Spincemaille, and Y. Wang, "perfusion quantification from multi delay arterial spin labeling(ASL): validation on neumerical ground truth."

[18] W. Huang, Q. Zhang, G. Wu, P. Pian Chen, J. Li, K. McCabe Gillen, P. Spincemaille, G. C. Chiang, A. Gupta, Y. Wang, and F. Chen, "DCE-MRI quantitative transport mapping for noninvasively detecting hypoxia inducible factor-1alpha, epidermal growth factor receptor overexpression, and Ki-67 in nasopharyngeal carcinoma patients," *Radiother Oncol*, Sep 27, 2021.

[19] Q. Zhang, P. Spincemaille, M. Drotman, C. Chen, S. Eskreis-Winkler, W. Huang, L. Zhou, J. Morgan, T. D. Nguyen, and M. R. Prince, "Quantitative transport mapping (QTM) for differentiating benign and malignant breast lesion: Comparison with traditional kinetics modeling and semi-quantitative enhancement curve characteristics," *Magnetic resonance imaging,* vol. 86, pp. 86-93, 2022.

[20] L. S. Szczepaniak, P. Nurenberg, D. Leonard, J. D. Browning, J. S. Reingold, S. Grundy, H. H. Hobbs, and R. L. Dobbins, "Magnetic resonance spectroscopy to measure hepatic triglyceride content: prevalence of hepatic steatosis in the general population," *American*

Journal of Physiology-Endocrinology and Metabolism, vol. 288, no. 2, pp. E462-E468, 2005.

[21] G. Vernon, A. Baranova, and Z. Younossi, "Systematic review: the epidemiology and natural history of non‐alcoholic fatty liver disease and non‐alcoholic steatohepatitis in adults," *Alimentary pharmacology & therapeutics,* vol. 34, no. 3, pp. 274-285, 2011.

[22] G. C. Farrell, and C. Z. Larter, "Nonalcoholic fatty liver disease: from steatosis to cirrhosis," *Hepatology,* vol. 43, no. S1, pp. S99-S112, 2006.

[23] L. Calzadilla Bertot, and L. A. Adams, "The natural course of non-alcoholic fatty liver disease," *International journal of molecular sciences,* vol. 17, no. 5, pp. 774, 2016.

[24] M. Benedict, and X. Zhang, "Non-alcoholic fatty liver disease: An expanded review," *World journal of hepatology,* vol. 9, no. 16, pp. 715, 2017.

[25] R. Jafari, S. Chhabra, M. R. Prince, Y. Wang, and P. Spincemaille, "Vastly accelerated linear least‐squares fitting with numerical optimization for dual‐input delay‐compensated quantitative liver perfusion mapping," *Magnetic resonance in medicine,* vol. 79, no. 4, pp. 2415-2421, 2018.

[26] S. Sourbron, "A tracer-kinetic field theory for medical imaging," *IEEE Trans Med Imaging,* vol. 33, no. 4, pp. 935-46, Apr, 2014.

[27] Q. Zhang, L. Zhou, J. Morgan, T. Nguyen, P. Spincemelle, and Y. Wang, "Quantitative Transport Mapping (QTM): Inverse Solution to a Voxelized Equation of Mass Flux of Contrast Agent in a Porous Tissue Model."

[28] L. O. Schwen, M. Krauss, C. Niederalt, F. Gremse, F. Kiessling, A. Schenk, T. Preusser, and L. Kuepfer, "Spatio-temporal simulation of first pass drug perfusion in the liver," *PLoS Comput Biol,* vol. 10, no. 3, pp. e1003499, Mar, 2014.

[29] C. Debbaut, P. Segers, P. Cornillie, C. Casteleyn, M. Dierick, W. Laleman, and D. Monbaliu, "Analyzing the human liver vascular architecture by combining vascular corrosion casting and micro‐CT scanning: a feasibility study," *Journal of anatomy,* vol. 224, no. 4, pp. 509-517, 2014.

[30] G. Peeters, C. Debbaut, A. Friebel, P. Cornillie, W. H. De Vos, K. Favere, I. Vander Elst, T. Vandecasteele, T. Johann, and L. Van Hoorebeke, "Quantitative analysis of hepatic macro‐ and microvascular alterations during cirrhogenesis in the rat," *Journal of anatomy,* vol. 232, no. 3, pp. 485-496, 2018.

[31] M. Daemen, H. Thijssen, H. Van Essen, H. Vervoort-Peters, F. Prinzen, H. S. Boudier, and J. Smits, "Liver blood flow measurement in the rat the electromagnetic versus the microsphere and the clearance methods," *Journal of pharmacological methods,* vol. 21, no. 4, pp. 287-297, 1989.

[32] S. Lorthois, F. Cassot, and F. Lauwers, "Simulation study of brain blood flow regulation by intra-cortical arterioles in an anatomically accurate large human vascular network. Part II: flow variations induced by global or localized modifications of arteriolar diameters," *Neuroimage,* vol. 54, no. 4, pp. 2840-2853, 2011.

[33] D. Kuzmin, "A guide to numerical methods for transport equations," 2010.

[34] Q. Fang, S. Sakadžić, L. Ruvinskaya, A. Devor, A. M. Dale, and D. A. Boas, "Oxygen advection and diffusion in a three dimensional vascular anatomical network," *Optics express,* vol. 16, no. 22, pp. 17530, 2008.

[35] T. Koh, S. Hartono, C. Thng, T. Lim, L. Martarello, and Q. Ng, "In vivo measurement of gadolinium diffusivity by dynamic contrast‐enhanced MRI: A preclinical study of human xenografts," *Magnetic resonance in medicine,* vol. 69, no. 1, pp. 269-276, 2013.

[36] M. Sørensen, "Hepatic blood volume is decreased in patients with cirrhosis and does not decrease further after a meal like in healthy persons," *Scandinavian Journal of Gastroenterology,* vol. 56, no. 10, pp. 1205-1209, 2021.

[37] M. A. Munteanu, G. A. Nagy, and P. A. Mircea, "Current management of NAFLD," *Clujul medical,* vol. 89, no. 1, pp. 19, 2016.

[38] M. Sayiner, A. Koenig, L. Henry, and Z. M. Younossi, "Epidemiology of nonalcoholic fatty liver disease and nonalcoholic steatohepatitis in the United States and the rest of the world," *Clinics in liver disease,* vol. 20, no. 2, pp. 205-214, 2016.

[39] P. Kanwar, and K. V. Kowdley, "The metabolic syndrome and its influence on nonalcoholic steatohepatitis," *Clinics in liver disease,* vol. 20, no. 2, pp. 225-243, 2016.

[40] I. Nalbantoglu, and E. M. Brunt, "Role of liver biopsy in nonalcoholic fatty liver disease," *World journal of gastroenterology: WJG,* vol. 20, no. 27, pp. 9026, 2014.

[41] M. Mapara, B. S. Thomas, and K. Bhat, "Rabbit as an animal model for experimental research," *Dental research journal,* vol. 9, no. 1, pp. 111, 2012.

[42] E. E. Stewart, X. Chen, J. Hadway, and T.-Y. Lee, "Correlation between hepatic tumor blood flow and glucose utilization in a rabbit liver tumor model," *Radiology,* vol. 239, no. 3, pp. 740-750, 2006.

[43] S. Favelier, T. Germain, P.-Y. Genson, J.-P. Cercueil, A. Denys, D. Krausé, and B. Guiu, "Anatomy of liver arteries for interventional radiology," *Diagnostic and interventional imaging,* vol. 96, no. 6, pp. 537-546, 2015.

[44] K.-H. Lee, E. Liapi, J. A. Vossen, M. Buijs, V. P. Ventura, C. Georgiades, K. Hong, I. Kamel, M. S. Torbenson, and J.-F. H. Geschwind, "Distribution of iron oxide–containing Embosphere particles after transcatheter arterial embolization in an animal model of liver cancer: evaluation with MR imaging and implication for therapy," *Journal of Vascular and Interventional Radiology,* vol. 19, no. 10, pp. 1490-1496, 2008.

[45] J.-F. Yang, Z.-H. Zhao, Y. Zhang, L. Zhao, L.-M. Yang, M.-M. Zhang, B.-Y. Wang, T. Wang, and B.-C. Lu, "Dual-input two-compartment pharmacokinetic model of dynamic contrast-enhanced magnetic resonance imaging in hepatocellular carcinoma," *World journal of gastroenterology,* vol. 22, no. 13, pp. 3652, 2016.

[46] E. Tsai, and T.-P. Lee, "Diagnosis and evaluation of nonalcoholic fatty liver disease/nonalcoholic steatohepatitis, including noninvasive biomarkers and transient elastography," *Clinics in liver disease,* vol. 22, no. 1, pp. 73-92, 2018.

[47] Y. Takahashi, and T. Fukusato, "Histopathology of nonalcoholic fatty liver disease/nonalcoholic steatohepatitis," *World journal of gastroenterology: WJG,* vol. 20, no. 42, pp. 15539, 2014.

[48] K. Vergesslich, M. Götz, G. Mostbeck, G. Sommer, and W. Ponhold, "Portal venous blood flow in cystic fibrosis: assessment by Duplex Doppler sonography," *Pediatric radiology,* vol. 19, no. 6-7, pp. 371-374, 1989.

[49] T. Koopman, R. M. Martens, C. Lavini, M. Yaqub, J. A. Castelijns, R. Boellaard, and J. T. Marcus, "Repeatability of arterial input functions and kinetic parameters in muscle obtained by dynamic contrast enhanced MR imaging of the head and neck," *Magnetic resonance imaging,* vol. 68, pp. 1-8, 2020.

[50] H. Tan, T. Liu, Y. Wu, J. Thacker, R. Shenkar, A. G. Mikati, C. Shi, C. Dykstra, Y. Wang, and P. V. Prasad, "Evaluation of iron content in human cerebral cavernous malformation using quantitative susceptibility mapping," *Investigative radiology,* vol. 49, no. 7, pp. 498, 2014.

[51] S. Zhang, G. C. Chiang, R. S. Magge, H. A. Fine, R. Ramakrishna, E. W. Chang, T. Pulisetty, Y. Wang, W. Zhu, and I. Kovanlikaya, "Texture analysis on conventional MRI images accurately predicts early malignant transformation of low-grade gliomas," *Eur Radiol,* vol. 29, no. 6, pp. 2751-2759, Jun, 2019.

[52] S. Saadeh, Z. M. Younossi, E. M. Remer, T. Gramlich, J. P. Ong, M. Hurley, K. D. Mullen, J. N. Cooper, and M. J. Sheridan, "The utility of radiological imaging in nonalcoholic fatty liver disease," *Gastroenterology,* vol. 123, no. 3, pp. 745-750, 2002.

[53] N. F. Schwenzer, F. Springer, C. Schraml, N. Stefan, J. Machann, and F. Schick, "Non-invasive assessment and quantification of liver steatosis by ultrasound, computed tomography and magnetic resonance," *Journal of hepatology,* vol. 51, no. 3, pp. 433-445, 2009.

[54] M. Sasso, I. Tengher‐Barna, M. Ziol, V. Miette, C. Fournier, L. Sandrin, R. Poupon, A. C. Cardoso, P. Marcellin, and C. Douvin, "Novel controlled attenuation parameter for noninvasive assessment of steatosis using Fibroscan®: validation in chronic hepatitis C," *Journal of viral hepatitis,* vol. 19, no. 4, pp. 244-253, 2012.

[55] J. K. Dyson, Q. M. Anstee, and S. McPherson, "Non-alcoholic fatty liver disease: a practical approach to diagnosis and staging," *Frontline gastroenterology,* vol. 5, no. 3, pp. 211-218, 2014.

[56] S. A. Müller, F. Pianka, M. Schöbinger, A. Mehrabi, H. Fonouni, B. Radeleff, H.-P. Meinzer, and B. M. Schmied, "Computer-based

This article has been accepted for publication in IEEE Transactions on Biomedical Engineering. This is the author's version which has not been fully edited and content may change prior to final publication. Citation information: DOI 10.1109/TBME.2022.3207057

> TBME-00011-2022 <
11

liver volumetry in the liver perfusion simulator," *Journal of Surgical Research,* vol. 171, no. 1, pp. 87-93, 2011.

[57] C. H. Thng, T. San Koh, D. J. Collins, and D. M. Koh, "Perfusion magnetic resonance imaging of the liver," *World Journal of Gastroenterology: WJG,* vol. 16, no. 13, pp. 1598, 2010.

[58] T. S. Koh, C. H. Thng, P. S. Lee, S. Hartono, H. Rumpel, B. C. Goh, and S. Bisdas, "Hepatic metastases: in vivo assessment of perfusion parameters at dynamic contrast-enhanced MR imaging with dual-input two-compartment tracer kinetics model," *Radiology,* vol. 249, no. 1, pp. 307-320, 2008.

[59] F. Calamante, M. Mørup, and L. K. Hansen, "Defining a local arterial input function for perfusion MRI using independent component analysis," *Magnetic Resonance in Medicine: An Official Journal of the International Society for Magnetic Resonance in Medicine,* vol. 52, no. 4, pp. 789-797, 2004.

[60] C. Cuenod, and D. Balvay, "Perfusion and vascular permeability: basic concepts and measurement in DCE-CT and DCE-MRI," *Diagnostic and interventional imaging,* vol. 94, no. 12, pp. 1187-1204, 2013.

[61] W. Yao, Y. Li, and G. Ding, "Interstitial fluid flow: the mechanical environment of cells and foundation of meridians," *Evidence-Based Complementary and Alternative Medicine,* vol. 2012, 2012.

[62] J. J. N. van Schie, C. Lavini, L. J. van Vliet, and F. M. Vos, "Estimating the arterial input function from dynamic contrast-enhanced MRI data with compensation for flow enhancement (I): Theory, method, and phantom experiments," *J Magn Reson Imaging,* vol. 47, no. 5, pp. 1190-1196, May, 2018.

[63] L. de Rochefort, T. Nguyen, R. Brown, P. Spincemaille, G. Choi, J. Weinsaft, M. R. Prince, and Y. Wang, "In vivo quantification of contrast agent concentration using the induced magnetic field for time-resolved arterial input function measurement with MRI," *Med Phys,* vol. 35, no. 12, pp. 5328-39, Dec, 2008.

[64] L. de Rochefort, T. Liu, B. Kressler, J. Liu, P. Spincemaille, V. Lebon, J. Wu, and Y. Wang, "Quantitative susceptibility map reconstruction from MR phase data using bayesian regularization: validation and application to brain imaging," *Magn Reson Med,* vol. 63, no. 1, pp. 194-206, Jan, 2010.

[65] S. Eskreis-Winkler, Y. Zhang, J. Zhang, Z. Liu, A. Dimov, A. Gupta, and Y. Wang, "The clinical utility of QSM: disease diagnosis, medical management, and surgical planning," *NMR Biomed,* vol. 30, no. 4, Apr, 2017.

[66] N. M. Khilnani, P. A. Winchester, M. R. Prince, E. Vidan, D. W. Trost, H. L. Bush, Jr., R. Watts, and Y. Wang, "Peripheral vascular disease: combined 3D bolus chase and dynamic 2D MR angiography compared with x-ray angiography for treatment planning," *Radiology,* vol. 224, no. 1, pp. 63-74, Jul, 2002.

[67] B. Xu, P. Spincemaille, G. Chen, M. Agrawal, T. D. Nguyen, M. R. Prince, and Y. Wang, "Fast 3D contrast enhanced MRI of the liver using temporal resolution acceleration with constrained evolution reconstruction," *Magn Reson Med,* vol. 69, no. 2, pp. 370-81, Feb, 2013.

[68] L. Feng, R. Grimm, K. T. Block, H. Chandarana, S. Kim, J. Xu, L. Axel, D. K. Sodickson, and R. Otazo, "Golden-angle radial sparse parallel MRI: combination of compressed sensing, parallel imaging, and golden-angle radial sampling for fast and flexible dynamic volumetric MRI," *Magn Reson Med,* vol. 72, no. 3, pp. 707-17, Sep, 2014.

[69] Y. Wang, and R. L. Ehman, "Retrospective adaptive motion correction for navigator-gated 3D coronary MR angiography," *J Magn Reson Imaging,* vol. 11, no. 2, pp. 208-14, Feb, 2000.

[70] Y. Wang, T. M. Grist, F. R. Korosec, P. S. Christy, M. T. Alley, J. A. Polzin, and C. A. Mistretta, "Respiratory blur in 3D coronary MR imaging," *Magn Reson Med,* vol. 33, no. 4, pp. 541-8, Apr, 1995.

[71] W. Qiu, D. Li, X. Jin, F. Liu, T. D. Nguyen, M. R. Prince, Y. Wang, and P. Spincemaille, "Sliding motion compensated low-rank plus sparse (SMC-LS) reconstruction for high spatiotemporal free-breathing liver 4D DCE-MRI," *Magn Reson Imaging,* vol. 58, pp. 56-66, May, 2019.

[72] T. Chikui, M. Obara, A. W. Simonetti, M. Ohga, S. Koga, S. Kawano, Y. Matsuo, T. Kamintani, T. Shiraishi, and E. Kitamoto, "The principal of dynamic contrast enhanced MRI, the method of pharmacokinetic analysis, and its application in the head and neck region," *International journal of dentistry,* vol. 2012, 2012.

[73] G. Brix, W. Semmler, R. Port, L. R. Schad, G. Layer, and W. J. Lorenz, "Pharmacokinetic parameters in CNS Gd-DTPA enhanced MR imaging," *Journal of computer assisted tomography,* vol. 15, no. 4, pp. 621-628, 1991.

[74] K. S. S. Lawrence, and T.-Y. Lee, "An adiabatic approximation to the tissue homogeneity model for water exchange in the brain: I. Theoretical derivation," *Journal of Cerebral Blood Flow & Metabolism,* vol. 18, no. 12, pp. 1365-1377, 1998.

[75] Z. Ahmed, and I. R. Levesque, "An extended reference region model for DCE‐MRI that accounts for plasma volume," *NMR in Biomedicine,* vol. 31, no. 7, pp. e3924, 2018.

[76] J. Cárdenas-Rodríguez, C. M. Howison, and M. D. Pagel, "A linear algorithm of the reference region model for DCE-MRI is robust and relaxes requirements for temporal resolution," *Magnetic resonance imaging,* vol. 31, no. 4, pp. 497-507, 2013.